Bioinspired Particle Engineering for Non-invasive Inhaled Drug Delivery to the Lungs

Snehal K. Shukla[1], **Apoorva Sarode**[2], **Dipti D Kanabar**[1], **Aaron Muth**[1], **Nitesh K Kunda**[1], **Samir Mitragotri**[2], **Vivek Gupta**[1,*]

[1]Department of Pharmaceutical Sciences, College of Pharmacy and Health Sciences St. John's University, Queens, NY 11439, USA

[2]Harvard John A. Paulson School of Engineering and Applied Sciences, Harvard University, Cambridge, MA 02138, USA

Abstract

Pulmonary drug delivery is governed by several biophysical parameters of delivery carriers, such as particle size, shape, density, charge, and surface modifications. Although much attention has been given to other parameters, particle shape effects have rarely been explored. In this work, we assess the influence of particle shape of inhaled delivery carriers on their aerodynamic properties and macrophage uptake by using polymeric microparticles of different geometries ranging in various sizes. Doxorubicin was conjugated to the polymer particles and the bioconjugates were characterized. Interestingly, the results of *in-vitro* lung deposition, performed using a next generation impactor, demonstrated a significant improvement in the aerodynamic properties of the rod-shaped particles with a high aspect ratio as compared to spherical particles with the same equivalent volume. The results of a macrophage uptake experiment demonstrate that the high aspect ratio particles were phagocytosed less than spherical particles. Furthermore, the cytotoxicity of these doxorubicin-conjugated particles was determined against murine macrophages, resulting in reduced toxicity when treated with high aspect ratio particles as compared to spherical particles. This project provides valuable insights into the influence of particle shape on aerodynamic properties and primary defense mechanisms in the peripheral lungs, while using polymeric microparticles of various sizes and geometries. Further systematic development can help translate these findings to preclinical and clinical studies for designing efficient inhalable delivery carriers.

Keywords

Particle shape; bioinspired; aspect ratio; aerodynamics; cellular uptake; inhalable carriers

*To whom correspondence should be addressed: Dr. Vivek Gupta, College of Pharmacy and Health Sciences, St. John's University, 8000 Utopia Parkway, Queens, NY – 11439. Phone: 718-990-3929. guptav@stjohns.edu.

1.0   Introduction

Non-invasive pulmonary drug delivery has been widely explored for localized delivery to the lungs and as a route for systemic drug delivery, due to the large surface area available for drug absorption [1]. Human lungs, however, have efficient defense mechanisms, such as mucociliary escalation in the central lung region (upper airways), and phagocytic uptake by alveolar macrophages in the peripheral lung region, to eliminate any inhaled foreign material and prevent its retention in the lungs [1–3]. Advances in the field of pulmonary drug delivery have identified several tunable bio-physical parameters that influence drug delivery to the lungs. Parameters such as particle size [4–6], density [7–9], rigidity [10,11], hygroscopicity [12–14] and surface chemistry [15–17] have been reported to govern the fate and deposition of inhaled particles in the lungs.

Despite these advancements, drug delivery to the lungs suffers from multiple limitations, such as low dose deposition, rapid elimination of inhaled particles by existing defense mechanisms, and short half-life, impacting drug bioavailability and poor patient compliance [7,18]. For efficient delivery to the lungs, inhaled delivery carriers must reach the desired site of action, which in most respiratory diseases is the peripheral lungs, while also evading phagocytic uptake by alveolar macrophages [1,19]. The importance of particle shape was highlighted by understanding the enhanced and prolonged retention of respiratory disease-causing microorganisms, such as *Mycobacterium tuberculosis*, *Hemophilus influenza*, *Legionella pneumophila* and *Pseudomonas aeruginosa* in the lungs [20–22]. While inhaled particulate delivery carriers are known to be rapidly eliminated from the lungs, these microorganisms demonstrate prolonged retention in the peripheral lungs after evading existing lung defense mechanisms, thereby resulting in severe respiratory diseases. Interestingly, the shape of these microorganisms is known to be aspherical or rod-like, which suggests that their shape plays an important role in enhancing their aerodynamic properties while also evading clearance from the lungs [23,24].

In addition to aspherical microorganisms, rod-shaped or fibrous particles such as asbestos and carbon nanotubes, are known to deposit in the alveolar region. This deposition causes adverse health effects, implying that particle shape enhances the aerodynamic behavior of particles [25,26]. Several computational fluid dynamic (CFD) studies have predicted the deposition performance of fibers or elongated particles in the lungs. Specifically, it is reported that they orient themselves parallel to the airflow, causing them to preferentially travel to the distal region of the lungs [27–29]. However, experimental respiratory deposition, or *in-vitro* deposition behavior, of such anisometric rod-shaped or fibrous particles, has not been thoroughly examined [30]. Thereby highlighting an opportunity to investigate the role of particle shape on the aerodynamic behavior and peripheral lung deposition of aspherical particles.

Along with particle deposition, macrophage internalization is another factor deciding the therapeutic fate of particles in the lungs. Several studies have highlighted the impact of particle shape on phagocytic uptake, with rod-shaped or filamentous particles being successful in evading phagocytic uptake [31–33]. It has been shown that cellular internalization is governed not only by the particle shape, but also by its orientation and

target geometry when interacting with the cell membrane. [31,34]. The target geometry of a particle is defined as the local shape of the particle (for aspherical particles) at the initial points of contact with the target cells [34]. Studies have reported that target geometry governs the local interaction between particles and macrophage surface, which further dictates the internalization of the particles [34–36]. Their results indicated that particles with low curvature regions escape uptake by macrophages significantly as compared to high curvature regions [32,34,37]. Therefore, fine-tuning the particle shape of inhaled delivery carriers may serve as a strategy to address the existing limitations of pulmonary drug delivery systems and improve their therapeutic efficiency.

The aim of the present study is to explore a novel strategy of particle shape modulation for developing effective inhaled delivery carriers possessing efficient aerodynamic properties for peripheral lung deposition, and evading macrophagic uptake. To this end, we have utilized doxorubicin hydrochloride (DOX) as a model drug to evaluate the influence of particle shape on the therapeutic effectiveness of delivery carriers. The aerodynamic properties of particles with various sizes and shapes were empirically evaluated using a next generator impactor (NGI), which is an *in-vitro* lung deposition simulator. Furthermore, the impact of particle shape on the cytotoxicity and uptake of various DOX-conjugated particles have been studied using RAW 264.7 murine macrophages.

2.0 Materials and Methods

2.1 Materials

Polybead® carboxylate microspheres of various sizes (0.5 μm, 6.0 μm and 10 μm) were purchased from PolySciences, Inc. (Warrington, PA, USA). Poly (vinyl alcohol) (PVA-fully hydrolyzed) was obtained from Sigma Aldrich (St. Louis, MO, USA). Doxorubicin hydrochloride (DOX) was procured from LC laboratories (Woburn, MA, USA). Phosphate buffered saline (PBS) pH 7.4, dimethyl sulfoxide (DMSO), and HPLC grade solvents (acetonitrile and water) were purchased from Fisher Scientific (Hampton, NH, USA). Various other assay kits and molecular biology grade reagents were obtained from several sources which have been listed along with their respective methods.

2.2 Cell Culture

RAW 264.7 murine macrophage cells were acquired from American Type Culture Collection (ATCC) (Manassas, VA, USA). RAW 264.7 cells were grown in Dulbecco's Modified Eagle's Medium (DMEM) (Corning Inc., Corning, NY, USA), supplemented with 10% fetal bovine serum (Atlanta Biologicals, Flowery Branch, GA, USA), 1% sodium pyruvate and 1% penicillin-streptomycin (Corning Inc., Corning, NY, USA) and incubated at 37°C under 5% CO_2. 3-(4,5-dimethylthiazol-2-yl)-2,5-diphenyltetrazolium bromide (MTT) and crystal violet were obtained from Fisher Scientific (Hampton, NH, USA). Vectashield hardset mounting medium kit with DAPI was procured from Vector Laboratories Inc. (Burlingame, CA, USA).

2.3   Particle Fabrication

Spherical polystyrene particles were fabricated to rod-shaped particles using a one dimension stretching method as previously reported with slight modifications [38]. As shown in Figure 1A, carboxylic acid-functionalized polystyrene particles of various sizes (0.5 μm, 6 μm and 10 μm) were dispersed into a polyvinyl alcohol (PVA) film and were subsequently stretched to the desired length in an oil bath using a custom made apparatus [38]. The detailed process is discussed in the subsequent sections i.e., 2.3.1, 2.3.2 and 2.3.3.

2.3.1   Film preparation—Briefly, 5% PVA w/V (~2 g in 30 ml of water) was dissolved in water at 85°C with continuous stirring. After complete dissolution of PVA, 2% (w/V) glycerol was added as a plasticizer to the PVA solution. The resultant mixture was then allowed to cool to room temperature and spherical polystyrene particles (~20 mg) were added to this mixture. The mixture was then carefully poured onto a 13 cm × 13 cm plastic petri dish (BIPEE®; 0708191706106; purchased from Amazon.com) to avoid trapping any air bubbles in the film. However, if bubbles were present in the film, they were carefully removed using micro pipette. The resultant films were dried completely for ~48 hours and stored in a dry place until further use.

2.3.2   Film stretching—The dried film was cut into ~5 × 5 cm sections and mounted on custom-made stretchers as described in Figure S1 [34,39]. The stretcher was comprised of two aluminum blocks mounted on a rotating screw. After mounting the film on the blocks, the length of the film (from block to block) was measured to determine the final stretching distance. The stretcher along with the mounted film was immersed in hot mineral oil (~120°C) for 5 minutes to liquefy the embedded polystyrene particles and stretching was performed while keeping the stretcher immersed in the oil bath (Figure 1A). Stretching of the film was performed to 3-fold or 6-fold of the initial length of the film mounted between aluminum blocks to obtain rod shaped particles of varied lengths. Short rods (SR) were obtained upon stretching the film to 3-fold of its initial length, while 6-fold stretching resulted in long rods (LR). After stretching to the desired distance, the film was cooled for 10 minutes before removal from the stretcher.

2.3.3   Particle recovery—The stretched film was removed from the stretcher and cut into small pieces which were dissolved in water at 70 °C. The particles were then washed 3x by centrifugation at 10,000×*g* for 10 minutes with water to remove PVA and residual oil from the mixture. The recovered stretched particles were finally redispersed in 1 mL of water and stored at 4 °C until further use.

2.4   Structural Morphology

Morphology of both spherical and stretched particles was examined using a Nova NanoSEM™ 450 and a Helios NanoLab 660 (FEI, Hillsboro, Oregon, USA). Briefly stated, the particles were dried on the SEM pin stub (Ted Pella, Inc., Redding, CA, USA) and then sputter coated with palladium for 90 seconds and imaged at 5 kV. Dimensions of the particles were obtained by measuring 30 particles from each of the obtained micrographs using Image J analysis software with n=3 images for each sample (total 90 particles/sample).

2.5   Conjugation of Doxorubicin (DOX) on Spherical and Stretched Particles

Conventional carbodiimide chemistry was used for conjugating the carboxylate groups on the particles' surface to the amine group of DOX, resulting in formation of an amide bond as shown in Figure 1B [40]. Briefly, 1 mg of particles were added to an aqueous solution containing an excess of 50mM 1-Ethyl-3-(3-dimethylaminopropyl) carbodiimide (EDC) and 25 mM N-hydroxy succinimide (NHS), and stirred for 5 hours at room temperature to activate the carboxylate groups on the particles' surface. The particles were then centrifuged to remove the excess EDC and NHS, followed by washing to ensure complete removal of the reagents. The activated particles were then incubated with an excess amount of DOX (1 mg) for 24 hours Following the incubation period, the unconjugated drug was separated by centrifugation at $10,000 \times g$ for 10 minutes followed by washing the particles twice with water. Additionally, the conjugated particles were washed with methanol to remove any free DOX. The DOX-conjugated particles were then resuspended in water and stored at 4°C for further analysis. Spheres of all sizes used for conjugation were also recovered from the PVA films, as described in 2.3.1, after placing them in the hot oil bath as mentioned in section 4.3 for the stretched particles. This was done to expose the carboxylic groups of spheres to similar conditions as that of SR and LR.

The amount of drug conjugated was determined by measuring the DOX absorbance of the intact conjugated particles at 485 nm using a TECAN Spark10M plate reader (Tecan Group Ltd., Männedorf, Switzerland).

2.6   Solid State Characterization of DOX Conjugation

DOX conjugation was characterized by DSC and FT-IR studies using freeze dried samples. Samples were lyophilized using a LABCONCO FreeZone freeze dryer (Kansas City, MO, USA). Freeze-dried samples were then stored at 4 °C in an air-tight container until further experiments were performed.

2.6.1   DSC studies—Calorimetric studies of DOX, blank 10 μm particles, a physical mixture of DOX and blank particles, and DOX-conjugated particles were performed using a DSC 6000 (Perkin Elmer; Waltham, MA, USA) equipped with an intra-cooler accessory. 1.5 mg of sample was sealed in an aluminum pan, while a sealed empty pan was maintained as reference. The samples were analyzed over a temperature range of 50 °C to 300 °C at a heating rate of 10°C/minute while being maintained under a nitrogen purge having a flow rate of 50 mL/minute.

2.6.2   FT-IR—FT-IR analysis of the samples was performed using a Spectrum-100 (Perkin Elmer, Inc.; Shelton, CT, USA) equipped with attenuated transmittance reflectance (ATR). The spectra of DOX, blank polystyrene particles, DOX-conjugated particles, and a physical mixture of DOX and blank particles were measured for comparison over the 1000–4000 cm^{-1} range.

2.6.3   UV-Visible Absorbance Studies—UV spectra of the samples were obtained using a TECAN Spark10M plate reader (Tecan Group Ltd., Männedorf, Switzerland).

Spectra of samples; Dox, blank polystyrene particles and DOX-conjugated particles were obtained by performing scan over the UV-visible range of 300–700 nm range.

2.6.4   Thermogravimetric Analysis (TGA)—TGA of blank polystyrene particles was performed using TGA7 (Perkin Elmer; Waltham, MA, USA) to confirm the residual moisture evaporation. About 5 mg of sample was weighed accurately and placed on a previously tared platinum pan. Sample was analyzed for % weight loss by heating at temperature ranging from 50°C to 300 °C maintained under a constant nitrogen purge of 20 mL/min.

2.7   *In-vitro* Pulmonary Deposition Behavior

Aerodynamic properties of the inhaled particles govern their *in-vitro* deposition behavior and can be used to estimate the lung deposition patterns of particles *in-vivo* [41]. The *in-vitro* deposition behavior of DOX-conjugated particles was assessed using a Copley-170 Next Generation Impactor™ (NGI, MSP corporation, MN, USA) to predict the effect of particle shape on aerodynamic properties using methods previously reported by our group [42,43]. Briefly, 2 mL of DOX-conjugated particles at a concentration of 450 μg/mL were nebulized using a jet nebulizer, PARI LC PLUS® nebulizer cup connected with Pari FAST-NEB compressor system into a pre-cooled impactor under vacuum maintained at 15 liters/minute for 4 minutes. The NGI was previously cooled at 4 °C for 90 minutes to avoid heat-transfer which otherwise may cause shrinkage of nebulized droplets, thereby impacting the particles' deposition behavior [44]. Following nebulization, particles deposited on each stage of the NGI were collected using a cell scrapper and analyzed for the amount of drug present using a TECAN Spark10M plate reader (Tecan Group Ltd., Männedorf, Switzerland), as described earlier. Aerodynamic parameters, such as fine particle fraction (% FPF) and mass median aerodynamic diameter (MMAD), were calculated from the amount of drug deposited in each stage as reported previously [45]. % FPF was determined as the fraction of emitted dose deposited in the NGI stages with < 5.39 μm, while MMAD (d_{ae} < 5.39 μm) represented the aerodynamic particle size distribution and was calculated using log-probability analysis (n = 3) [43].

2.8   *In-vitro* Release Studies

In-vitro release studies of all 10 μm DOX-conjugated particles (spheres, short rods, long rods) were performed using a release method previously reported with slight modifications [16]. Briefly, 2 mg of DOX-conjugated particles were dispersed in 5 mL of PBS pH 7.4 and acetate buffer pH 5.5. The samples were incubated at 37 °C with continuous shaking at 50 rpm. At predetermined intervals, the samples were centrifuged at 10,000×g for 10 minutes, and obtained supernatants were analyzed at a wavelength of 485 nm using a TECAN Spark10M plate reader to determine the amount of DOX released.

2.9   Stability Studies

Stability studies of 10 μm DOX-conjugated particles were performed by storing the samples at two different conditions: 4 °C (representing normal refrigerated storage) and 40 °C/75%RH (accelerated stability storage) for a time interval of 15 days as reported previously [46,47]. Following the storage period, the samples were analyzed in terms of particle size

along with aspect ratio, change in particle shape and amount of DOX-conjugated as μg of Dox/mg of particles.

2.10 Cytotoxicity Assessment

Cytotoxicity studies of free DOX and DOX-conjugated 10 μm particles were performed against RAW 264.7 murine macrophages using the MTT assay. Briefly, RAW 264.7 macrophages were seeded at a density of 2.5×10^3 cells/well in tissue culture treated 96-well plates (Eppendorf, Hauppauge, NY, USA) and were incubated overnight at 37 °C/5% CO_2. Cells were then treated with the various DOX-conjugated particles or free DOX and were incubated for 24 hours or 48 hours. After their respective treatment period, media was removed and the MTT dye (1 mg/mL) was added followed by 2 hours of incubation. DMSO was then added to each well after aspirating the MTT solution to dissolve the formazan crystals formed during MTT incubation. The plates were then shaken for 30 minutes on a plate shaker and the optical absorption was measured at 570 nm using a TECAN Spark10M plate reader (Tecan Group Ltd., Männedorf, Switzerland). The cytotoxicity of the particles was determined by comparing the cell viability against the non-treated cells used as control groups. IC_{50} values were determined by normalizing and transforming the data to log values using GraphPad Prism Software Version 6.0.

2.11 Cellular Uptake Studies

The uptake of different shaped DOX-conjugated particles and free DOX was evaluated in RAW 264.7 murine macrophages using a previously reported method [48]. Briefly, 1.0×10^4 cells/chamber were seeded on an 8-chambered imaging coverslip (Eppendorf, Hauppauge, NY, USA) and were incubated overnight at 37 °C and 5% CO_2. The cells were then treated with DOX-conjugated particles or free DOX (2.9 μg/mL) for 3 hours; and were subsequently washed twice with ice-cold PBS (1X). The cells were then fixed using 4% paraformaldehyde for 10 minutes and then again washed with PBS (1X) to remove excess paraformaldehyde. The coverslip was separated from the chamber and it was mounted on a clear glass microscopic slide using a VECTASHEILD hardset mountant containing DAPI (H1500, Vector laboratories, Burlingame, CA, USA). The cells were then imaged using an EVOS-FL fluorescence microscope (Thermo Fisher Scientific, Waltham, MA, USA) at 20X magnification.

In addition to a qualitative assessment, intracellular quantification of DOX was also performed according to a previously published method [48]. Briefly, RAW 264.7 macrophages were seeded at a density of 1.0×10^6 cells/well in 6-well plates and incubated overnight at 37 °C and 5% CO_2. The cells were then treated with DOX and DOX-conjugated 10 μm particles for 1 hour or 3 hours. After the respective time interval, the treatment solution was aspirated, and cells were washed twice with ice-cold PBS (1X). The cells were harvested using a cell scraper and centrifuged to obtain a cell pellet. The obtained pellet was washed twice using 1X PBS and was lysed using 100 μL DMSO. The lysed pellet was centrifuged again, and the obtained supernatant was subjected to fluorometric analysis. The florescence intensity of DOX in each treatment group was determined at an excitation wavelength of 480 nm and an emission wavelength of 590 nm using a TECAN Spark10M plate reader (Tecan Group Ltd., Männedorf, Switzerland) [49].

2.12   Statistical Analysis

All results are presented as a mean ± SD unless otherwise stated. Statistical significance was determined using the student's t-test, one-way ANOVA and Tukey's post-hoc multiple comparison by GraphPad Prism 6.01 (San Jose, CA, USA). $p<0.05$ or less was considered significant.

3.0   Results and Discussion

3.1   Particle Fabrication and Morphology of Particles

Three different polystyrene particle sizes were used to prepare elongated rod-shaped (fiber-like) particles. The rod-shaped particles were successfully fabricated using one-dimensional film stretching as mentioned in the methods section. Both spherical and stretched particles were imaged using scanning electron microscopy (SEM). As shown in Figure 2, spherical particles of various sizes were successfully transformed to rod-shaped particles with varied aspect ratios. The aspect ratio (AR) is defined as the ratio of the length of the major axis of the particles to the length of the minor axis of the particles. As observed in Table 1 and Figure 2, 3-fold stretching of 0.5 μm particles resulted in short rod (SR) shaped particles with a major axis of 1.4±0.1 μm and a minor axis 0.3±0.0 μm resulting in an AR of 4.1±0.2.

Further stretching the particles 6-fold resulted in 0.5 μm particles producing long rods (LR) with a major axis length of 1.9±0.2 μm and minor axis length of 0.3±0.0 μm, resulting in an AR value of 6.6±0.6. An increase in stretching length then resulted in an increase in the AR value. Similarly, 6.0 μm polystyrene particles which underwent 3-fold stretching resulted in an SR with 9.1±0.9 μm (major axis length) and 1.7±0.3 μm (minor axis length) causing an AR value of 5.4±0.8. Furthermore, LR of 6.0 μm equivalent diameter displayed 13.7±1.6 μm (major axis length) and 1.5±0.4 (minor axis length) resulting in 9.1±1.4 AR (Table 1 and Figure 2). Stretching of 10.0 μm particles 3-fold resulted in fabrication of SR particles with a 22.1±3.3 μm major axis length and a 7.1±0.9 μm of minor axis length accounting for an AR value of 3.3±0.5. Similarly, stretching to 6-fold formed LR particles with 32.2±3.2 μm (major axis length) and 5.6±0.9 μm (minor axis length) resulting in a 5.8±1.1 AR value as shown in Table 1 and Figure 2. AR values of both SR and LR particles stretched from their 10.0 μm diameter size was found to be less than their respective counterparts of 6.0 μm and 0.5 μm diameter size particles. This reduction in AR values can be attributed to the increased rigidity of the particles with an increase in equivalent diameter [50]. These results suggest that particles of various sizes can be successfully transitioned from spherical to rod shape by employing the described stretching method.

3.2   Conjugation of Drug (Doxorubicin) with Spherical and Stretched Particles

Doxorubicin (DOX) was chosen as the model drug for conjugation for the following major reasons: 1) widely explored conjugation chemistry and 2) inherent florescence which can be used for *in-vitro* assays. Fabricated particles were conjugated with DOX using EDC-NHS chemistry (Figure 1B); and the amount of DOX conjugated to the particles was analyzed by measuring the UV absorbance of the intact conjugated particles. As seen in Figure 3A, the amount of DOX conjugated to the particles remained relatively consistent, irrespective of size and shape of the particles. For example, the amount of DOX conjugated (μg of DOX/mg

of particles) with 0.5 μm particles was found to be 454.6±2.0 μg/mg (Sph), 469.1±5.3 μg/mg (SR) and 425.8±5.5 μg/mg (LR) (Figure 3A).

Further increasing the particle size to 6- and 10-μm resulted in the conjugation efficiency of DOX to polystyrene particles to be unaffected. For example, the 10 μm-Sph demonstrated a DOX conjugation of 425.5±3.3 μg/mg (μg of Dox/mg of particles). The stretched particles 10 μm-SR displayed 406.1±1.2 μg/mg, while 10 μm-LR demonstrated 399.0±1.9 μg/mg DOX being conjugated (Figure 3A). A similar amount of DOX conjugated/mg of particles in spherical as well as both the rod-shaped particles indicates that the carboxylic acid functionalized on the polystyrene particles remains unaffected by the stretching procedure. The number of carboxylic acid groups available for conjugation on the particles is dependent on the total particle volume indicating that an increase in size of the particle causes an increase in the number of carboxylic acid groups [50]. Therefore, to equalize the number of carboxylic acid groups available for conjugation amongst the particles of various size and shapes, we have used a constant total mass of particles for the conjugation reaction.

3.3   Characterization of DOX Conjugation

3.3.1   DSC Studies—Calorimetric studies were performed to evaluate the conjugation of DOX with the particles. Figure S2A is the representative thermogram of analyzed samples for 10 μm size particles. As can be observed, DOX showed a sharp endothermic peak at 206.2 °C, representing the melting of DOX as also reported in the literature [51,52]. DSC curve of PVA demonstrated an endotherm at 228°C which represents the meting point of the polymer as also reported previously [53]. The thermogram of blank particles displayed a small endothermic peak at 103.2 °C, representing the evaporation of residual water from the sample as confirmed by the TGA studies seen in Figure S2B. The thermal study results of the physical mixture of DOX and blank particles demonstrated endothermic peak at 198.4 °C, representing the melting point of DOX (Figure S2A). For all the DOX-conjugated particles, the characteristic peak of DOX was found to be absent, indicating that pure unbound DOX was not present in the conjugated particles and was removed during washing steps suggesting that DOX present in the formulation is conjugated to the particles. The obtained results are in accordance with previously published studies where the endothermic peak of DOX was found to be absent upon conjugation [52,56]. Therefore, it can be inferred that DOX was bound strongly to the particles resulting in the formation of a stable covalent bond.

3.3.2   FT-IR studies—The FT-IR spectra of analyzed samples are displayed in Figure 3C where DOX displayed several characteristic peaks at 3315 cm^{-1} (-N-H stretching), 2916 and 2898 cm^{-1} (-C-H stretching of phenyl rings), 1730 cm^{-1} (-C=O ketone stretching and C-H$_2$ bending), 1617 cm^{-1} (-CO-H bending), 1580 cm^{-1} (-C=O quinone stretching), 1525 cm^{-1} (out of plane vibration of -N-H) and 881 cm^{-1} (-C-N bending) [57–59]. Polystyrene particles demonstrated peaks at 3106 cm^{-1}, 3079 cm^{-1} and 3026 cm^{-1} (C-H stretching of aromatic rings and -O-H stretching of carboxylic acid), 2930 cm^{-1} and 2849 cm^{-1} (-CH$_2$- stretching), 1620 cm^{-1} ,1511 cm^{-1} and 1470 cm^{-1} (C=C stretching of aromatic rings) [60,61] (Figure 3C). Analysis of all three DOX-conjugated particles (10 μm-Sph, 10 μm-SR and 10 μm-LR) demonstrated a majority of the characteristic peaks of DOX

at ~3315 cm^{-1}, 2916 cm^{-1}, 1730 cm^{-1} and 1580 cm^{-1}, indicating the presence of DOX in the conjugated particles. However, as shown in Figure 3C, conjugation of DOX to polystyrene resulted into substitution of 1525 cm^{-1} (out of plane vibration of -N-H) of DOX with peak at 1509 cm^{-1} (10 μm-Sph), 1502 cm^{-1} (10 μm-SR) representing amide II vibrations of -N-H and -C-N stretching, indicating the involvement of the -NH$_2$ group to form the -CONH bond [56,62]. Amide vibrations observed in FT-IR spectra are reported as amide I, amide II and amide III vibrations. Amide I vibration is observed between 1600 cm^{-1}–1800 cm^{-1} and is majorly governed by -C=O stretching vibrations. Amide II vibrations are observed at 1470 cm^{-1} to 1570 cm^{-1} and are caused due to -N-H stretching and -C-N stretching vibrations while amide III is observed at 1250 cm^{-1} to 1350 cm^{-1} due to -C-H and -N-H deformation vibration [58,63]. In the FT-IR analysis performed for DOX conjugated particles, we observed amide II vibration while amide I and amide III vibrations were found to be absent. These FT-IR results indicate successful conjugation of DOX to the polystyrene particles via amide bond linkage between the carboxylic acid (-COOH) groups of polystyrene particles and amine (-NH$_2$) group of DOX.

3.3.3 UV-Visible Absorbance Studies—UV-Visible absorbance spectra of analyzed samples are shown in Figure S2C. As can be observed, blank polystyrene particles did not demonstrate any wavelength absorption in the analyzed UV-visible wavelength range of 300–700 nm. DOX exhibits a maximum wavelength (λ_{max}) absorption at 485 nm as in Figure S2C. However, upon conjugating DOX to polystyrene particles, the maximum wavelength (λ_{max}) for absorption shifted to 508 nm signifying a reduced energy state. This increase in λ_{max} is indicative of interaction between DOX and polystyrene particles during the conjugation process resulting into reduced energy state. Such change in the λ_{max} due to interactions between DOX and polymers have been previously reported [64,65]. Formation of the desired amide bond would result in this increased conjugation, resulting in the increased maximum wavelength of absorption. This finding is in accordance with our previous findings as described in the results of DSC and FTIR experiments.

3.4 *In-vitro* Pulmonary Deposition Behavior

Therapeutic delivery to the lungs through inhalation improves treatment efficacy due to localized accumulation and minimal exposure to other organs, subsequently reducing adverse effects [41]. As briefly discussed in Section 1.0, delivery of inhaled particles to the respiratory surface is governed by the aerodynamic properties of the particles; such as mass median aerodynamic diameter (MMAD) and % fine particle fraction (% FPF). For efficacious treatment, it is essential that the inhaled delivery carriers reach the desired site of action while also having an optimally controlled deposition rate at those sites [66]. The aerodynamic properties reflect the deposition behavior of the inhaled particles and provide valuable information about the respirability of the particles [45]. For optimal deep lung deposition of inhalable delivery carriers, an MMAD value of 1–5 μm is desired [8,67]. The aerodynamic behavior of the fabricated particles was assessed using a next generation cascade impactor (NGI); and is represented in terms of MMAD and % FPF. NGI comprises of eight impaction stages (stage 1 to stage 8) with decreasing nozzle size resulting in size fractionation stages representing the anatomical features of the human lungs for classifying the particles based on their aerodynamic properties [68]. The Copley-170 NGI™ consists of

various stages with different aerodynamic cut-off diameters (d_{ae}) reflecting different regions of the human respiratory tract. For example; stage 1 (d_{ae} 14.1 μm), stage 2 (d_{ae} 8.6 μm) and stage 3 (d_{ae} 5.4 μm) represent the upper respiratory tract (i.e., oropharyngeal region), while stage 4 to stage 8 represents d_{ae} 3.3 μm to 0.98 μm, reflecting the bronchoalveolar region [69]. The impact of particle shape and size on *in-vitro* pulmonary deposition is shown in Table 2.

The aerodynamic parameters of all stretched particles are presented in Table 2. A graphical presentation of the aerodynamic behavior of 10 μm particles is shown in Figures 4A & 4B, while a graphical representation of 0.5 μm and 6.0 μm particles are presented in the supplementary data (Figure S3). As a general trend, both the mass median aerodynamic diameter (MMAD), and fine particle fraction (FPF) appeared to change favorably with an increased aspect ratio (AR) of the particles (i.e., decrease in MMAD and increase in FPF), with effects of shape change more evident for bigger particle sizes (10 μm) (Table 2, Figures 3A & 3B). For example, all three 0.5 μm particles (0.5μm-Sph, 0.5μm-SR and 0.5μm-LR) demonstrated an MMAD of ~4.5 μm with no significant difference observed in % FPF with a value reported to be >75% (Figures S3A and S3B). An increase in particle size from 0.5 μm to 6.0 μm resulted in increase in the MMAD for 6.0μm-Sph (5.6±0.1 μm), along with a % FPF value of 61.7±2.1%, therefore making the particles non-respirable with maximum deposition occurring in the proximal region of the respiratory tract. However, a transition of particle shape from spheres to rods resulted in a significant (p<0.01) reduction in the MMAD value with a 4.3±0.2 μm for 6.0 μm-SR, and 4.7±0.1 μm for 6.0μm-LR (Table 2, Figures S3C and S3D). Interestingly, % FPF values for 6.0 μm rod-shaped particles were found to be significantly (p<0.05) increased as compared to spherical particles, as shown in Table 2 (76.2±1.1% FPF for 6.0μm-LR vs 61.7±2.1% for 6.0μm-Sph). Similarly, the MMAD value for 10 μm-Sph (Table 2) indicated a high MMAD value of 8.2±0.8 μm, while the stretched particles demonstrated significantly (p<0.0001) lower MMAD values of 4.2±0.6 μm for 10 μm-SR particles and 3.4±0.1 μm for 10 μm-LR particles. Upon comparing the % FPF values (Table 2), the 10 μm-Sph displayed ~45%, while rod-shaped particles demonstrated a significant (p<0.0001) increase in % FPF ,with ~90% for 10 μm-SR and ~95% for 10 μm-LR particles. This increase in % FPF indicates that most of the emitted dose will be deposited into the respirable region of the lungs which is comprised of the bronchi-alveolar region.

Deposition of 10 μm DOX-conjugated particles at various stages of NGI are illustrated in Figure 4A. For 10μm-Sph particles, deposition was observed mostly in stage 1 (~4 μg), stage 2 (~6 μg), stage 3 (~5 μg) and stage 4 (~3 μg) while   1 μg DOX deposition was observed from stage 5 to stage 8, indicating preferential accumulation above the bronchoalveolar regions. This indicates that the particles deposit primarily in the larger respiratory airways and will be cleared either by mucociliary clearance or exhalation [70]. Spherical particles do not appear to streamline themselves effectively and tend to deposit in the respiratory airways by various mechanisms based on their MMAD values; i.e., inertial impaction (for MMAD>5 μm), gravitational sedimentation (for MMAD 1 to 5 μm) or diffusion (for MMAD   0.5 μm) [71–73]. While stretched particles, 10 μm-SR and 10 μm-LR, , showed minimal deposition at stages 1 and 2 (1 μg). Deposition of stretched particles, both SR and LR, increased dramatically from stage 3 onwards. Maximum deposition of stretched particles was observed

in stage 5 where ~22 μg of DOX was quantified for 10 μm-SR and ~28 μg DOX for 10 μm-LR particles. At stage 6, the deposition of DOX decreased to ~16 μg for 10 μm-SR, while the reduction in deposition behavior of 10 μm-LR particles was mild, with ~25 μg DOX observed for 10 μm-LR. The deposition of 10 μm-LR particles, as shown in Figure 4A, continued until stage 8, with ~5 μg DOX observed, while the 10 μm-SR particles displayed ~0.5 μg DOX. Since the majority of the deposition for 10 μm-SR and 10 μm-LR stretched particles occurred after stage 3, this indicates that deposition of the particles will predominantly occur in the lower respiratory airways, such as the bronchoalveolar region, as represented by stages 4–8 of the NGI. Therefore, it can be confirmed that a change in particle shape enhanced their deposition into the deeper (peripheral) lungs. This can be attributed to better propulsion of rod-shape particles down the respiratory tract after properly aligning themselves with the air flow direction [28]. Several computational fluid dynamics (CFD) simulation models have predicted deposition of fibers (elongated rod shaped; AR>3) vs sphere particles in the lungs, where elongated particles are shown to streamline themselves with the air flow and deposit in the peripheral airways [27–29]. Rod-shaped particles deposit by interception, where the fiber-like particles come in close contact with the surface, which would have been missed by the center of the mass [74]. An increase in particle length results in an increase in particle deposition via interception, which allows the particles to properly align with the airflow and travel to the distal (peripheral) airways in the alveolar region [75]. This corroborates the improved aerodynamic behavior of rod-shaped particles as compared to spheres, and that amongst the rod-shaped particles, LR was better than SR. The % cumulative deposition plot, as shown in Figure 4B, indicated that 50% of the cumulative dose for the 10 μm-Sph deposited at the effective cut-off aerodynamic diameter of 5.57 μm. The stretched particles demonstrated a significantly (*p<0.0001*) lower effective cut-off aerodynamic diameter for 50% cumulative deposition: 2.53 μm for 10 μm-SR particles and 2.26 μm for 10 μm-LR particles (Figure 4B). Similar deposition behavior was observed for the 0.5 μm and 6.0 μm rod-shaped particles (Figure S3). The results presented in Figures 4A & 4B suggest that rod-shaped particles (stretched particles) significantly improved the aerodynamic deposition of the particles as compared to the spherical particles, resulting in maximum deposition into the alveolar region of the lungs. Therefore, the *in-vitro* pulmonary deposition results support the hypothesis that changing the shape of spherical particles to a rod-shape causes deeper lung deposition of particles.

3.5 *In-vitro* Release of DOX-conjugated Particles

The release of DOX from conjugated polystyrene particles was analyzed in buffer systems at pH 7.4, mimicking physiological conditions, and pH 5.5, representing intracellular lysosomal vesicles as well as the microenvironment of cancer cells [76,77]. As seen in Figure 4C, no burst release of DOX was observed in the *in-vitro* release study. The release of DOX was observed to be pH dependent, which indicated that the release of DOX was faster at lower pH values (i.e., 5.5) as compared to higher pH values (i.e., 7.4). Upon incubation at pH 5.5, DOX-conjugated particles released about 45.2±2.8 % of DOX from 10 μm-Sph particles, 43.8±1.3 % DOX from 10 μm-SR particles, and 45.7±1.3% DOX from 10 μm-LR particles after 5 days (Figure 4C), while a significantly (*p<0.0001*) small amount of DOX was found to be released at physiological pH 7.4, likely due to slower

hydrolysis of the amide bond [62]. At pH 7.4, the % drug released after 5 days of incubation was as follows: 10 μm-Sph particles observed 18.9±2.3% drug release, 10 μm-SR particles displayed 18.7±3.0% drug release, and 10 μm-LR particles showed 18.7±3.7% drug release (Figure 4C). The increased release of DOX from the particles at an acidic pH (5.5) is known to be mediated by cleavage of the amide bond by acid hydrolysis resulting in the subsequent release of DOX into the media [62,76]. These results are in accordance with other studies where a slower release of DOX was observed at pH 7.4 due to the enhanced stability of the amide conjugated DOX particles as well as slower hydrolysis kinetics at normal physiological conditions [62,77–79]. In addition, the slower release of DOX at physiological pH supports the use of these conjugated particles as effective delivery carriers due to a reduced loss of DOX while reaching the site of action, resulting in reduced off-target side effects and increased target accumulation [80,81]. However, unlike physiological conditions, these studies were performed in the absence of enzyme and therefore may not truly reflect the release mechanics of the drug from the particles.

3.6 Stability Studies

The stability of 10 μm DOX-conjugated particles was determined after storing for 15 days at two different conditions: 1) storage conditions represented by 4°C; and 2) accelerated stability conditions represented by 40°C and 75% relative humidity (RH), as previously reported [47]. The stability was assessed in terms of particle shape, particle size, and the amount of drug conjugated. Figure 5A shows representative SEM images of the particles, where no change was observed in the shape of the particles when stored at accelerated conditions as compared to normal storage conditions. This can be attributed to the high glass transition temperature (110°C) and non-biodegradability of polystyrene particles, which helps in retaining their shape at accelerated conditions (40°C/75% RH). Furthermore, the size of the stretched particles was measured using ImageJ software. As seen in Figure 5B, the major axis of the 10 μm-SR particles at 4 °C was found to be 25.2±1.2 μm and 24.6±1.9 μm at 40°C/75%RH (vs. 25.6±1.5 μm on Day 0). However, the minor axis of 10 μm-SR particles at 4 °C was 7.2±0.8 μm, and at 40°C/75%RH was 7.9±0.9 μm as compared to 7.5±0.7 μm on Day 0. The aspect ratio of the particles also showed a non-significant difference with 3.5±0.4 at normal conditions and 3.2±0.5 at accelerated conditions, vs. 3.4±0.3 on the initial day. Similarly, 10 μm-LR particles also displayed non-significant changes in particle size and aspect ratio (Figure 5B). The length of the major axis at 4 °C was found to be 36.2±2.0 μm, while at 40°C/75%RH it was reported to be 36.7±2.5 μm (vs. 36.5 ± 3.5 μm on day 0). The minor axis of 10 μm-LR particles at normal conditions was found to be 6.1±0.9 μm, and 5.9±0.9 μm at accelerated conditions, as compared to 6.0 ± 0.8 μm for day 0. Upon analyzing the aspect ratio values, no significant differences were observed at 4 °C with 6.4±1.0, 40°C/75%RH having 6.3±1.2 and day 0 with 6.1 ± 0.9 (Figure 5B).

The amount of DOX conjugated to the particles was also analyzed at the end of the stability period. As seen in Figure 5C, 10 μm-Sph displayed 426±10 μg of DOX/mg of particles at 4 °C and 421±9 μg of DOX/mg of particles at 40°C/75%RH as compared to 425±3 μg of DOX/mg of particles on Day 0. 10 μm-SR particles demonstrated 425±10 μg of Dox/mg of particles on day 0, and ~430 mg of μg of Dox/mg of particles at both stability conditions.

Similarly, 10 μm-LR particles displayed 455±8 μg of Dox/mg of particles on day 0, and non-significant changes with ~460 μg of Dox/mg of particles at both stability conditions (Figure 5C). These non-significant differences in the amount of conjugated drug present at both stability conditions can be attributed to the stable amide bond conjugation between DOX and the carboxylic acid of the polystyrene particles, which remains unaffected at increased temperatures [82]. These results indicate the superior stability of DOX-conjugated particles at accelerated conditions.

3.7. Cytotoxicity Assessment on Macrophages

The cytotoxicity of free DOX and DOX-conjugated particles (Sph, SR, and LR) was assessed against RAW 264.7 cells using an MTT assay at both 24- and 48-hours incubation. Figure 6A represents the % cell viability of RAW 264.7 cells after 24 hours treatment with 10 μm particles as compared to plain DOX. Free DOX demonstrated the highest cytotoxicity toward macrophages with an IC_{50} value of 1.06±0.1 μM. The DOX-conjugated spherical particles displayed ~70% cell viability at 5μM, while stretched particles SR and LR displayed ~75% cell viability (Figure 6A), and plain DOX demonstrated 27.1±4.1% cell viability at a concentration of 5μM. This data represents a ~2.5-fold reduction in the off-target toxicity of DOX when encapsulated in stretched inhalable particles.

DOX displayed a time-dependent cytotoxicity against macrophages as shown in Figure 6B and Table 3 with an IC_{50} value of 0.08±0.03 μM following 48 hours incubation. Treatment with DOX-conjugated 10 μm-Sph resulted in a ~28-fold increase in IC_{50} value; 2.8±0.8 μM, as compared to plain DOX. The stretched 10 μm-SR particles displayed a ~31-fold increase in IC_{50} value as compared to free DOX. Interestingly, treatment with 10 μm-LR particles resulted in a significant ($p<0.01$) ~71-fold increase in IC_{50} against DOX with a calculated IC_{50} of 7.5±3.1 μM. Additionally, 10 μm-LR particles displayed ~2.7-fold ($p<0.05$) increase in IC_{50} as compared to 10 μm-Sph, and ~2.5-fold ($p<0.05$) increase against 10 μm-SR particles (Figure 6B and Table 3). Similar results were also observed for various particles of 6.0 μm equivalent diameter (Figure S4). Based on these cytotoxicity results, the treatment groups can be ranked in the following order of reducing toxicity/increasing safety against RAW 264.7 macrophages: 10 μm-LR particles showing the highest safety, followed by 10 μm-SR particles, then 10 μm-Sph, and minimal safety was displayed by DOX .

The cytotoxicity of blank particles was also assessed in RAW 264.7 cells after 24- and 48-hours incubation. As seen in Figure 6C, after 24 hours of incubation, all blank particles demonstrated >85–90% cell viability. Similar results were also observed after 48 hours incubation of these particles as shown in Figure 6D, indicating that the particles were safe against RAW 264.7 cells. These findings indicate that the cytotoxicity of DOX-conjugated particles against macrophages is due to the DOX from the conjugated particles becoming internalized by the cells, and not due to the polystyrene particles.

3.7 Cellular Uptake – Investigating Escape of Particles by Macrophages

The intracellular uptake of DOX-conjugated spherical and stretched particles was analyzed for RAW 264.7 murine macrophages using a fluorescent microscope after incubation of particles for 3 hours. Macrophage clearance serves as a primary defense mechanism in

the deep lungs, and it is essential for inhalable delivery carriers to evade this uptake (phagocytosis) in order to result in prolonged retention upon deposition and improved efficacy of the treatment [1]. Cytotoxicity data of DOX and DOX-conjugated particles against RAW 264.7 macrophages revealed that an increase in the aspect ratio of the particles resulted in reduced toxicity to macrophages, indicating that particular shape plays an important role in cellular internalization. Therefore, we performed cellular uptake studies to evaluate the influence of particle shape on internalization by macrophages. As seen in Figure 7A (inset magnified image), DOX demonstrated significant internalization in RAW 264.7 murine macrophages with DOX fluorescence (Red) overlapping with the nuclei (DAPI - blue fluorescence). This indicates that free DOX was readily localized in the nuclei of RAW 264.7 cells. For 10 μm-Sph particles, it can be observed that DOX was conjugated to the spherical particles and distributed in the cytoplasm surrounding the nuclei of RAW 264.7 cells, as observed in the inset image (Figure 7A). The stretched particles 10 μm-SR displayed the presence of some DOX particles in the cytoplasm. However, the florescence intensity of DOX was comparatively less than the spherical particles, indicating reduced cellular uptake of the 10 μm-SR stretched particles as shown in the enlarged inset image (Figure 7A). For 10 μm-LR particles, the florescence intensity of DOX was found to be diminished, showing minimal DOX florescence in the cytoplasm or nuclei of the cells (Figure 7A). Therefore, an increase in the aspect ratio of the particle resulted in reduced internalization of DOX-conjugated particles, suggesting that particle shape impacts cellular uptake by macrophage cells. Based on these results, it can be inferred that a change in the shape of particles may influence their uptake by macrophages.

The intracellular uptake of free DOX and DOX-conjugated particles was also quantified by analyzing the fluorescence of DOX. As demonstrated in Figure 7B, free DOX displayed the highest florescence intensity at incubation times of 1- and 3-hours. Furthermore, free DOX demonstrated a significantly ($p<0.001$) higher fluorescence intensity than 10 μm particles (spherical and stretched) at both 1 hour and 3 hours of incubation. Amongst the10 um particles, Sph demonstrated a significantly higher florescence intensity after 1 hour incubation ~1.7-fold ($p<0.05$) and ~2.4 fold ($p<0.01$), than 10 μm-SR and 10 μm-LR particles, respectively. However, at 1 hour incubation, there was no significant difference observed between the fluorescence intensity of 10 μm-SR particles and 10 μm-LR particles. The fluorescence intensity of 10 μm-sphere particles after 3 hours of incubation displayed a ~1.4-fold ($p<0.01$) increase in florescence intensity as compared to 10 μm-SR particles, and ~2.4-fold ($p<0.001$) increase as compared to 10 μm-LR particles as shown in Figure 7B. Additionally, 10 μm-SR particles displayed a significantly ($p<0.01$) higher fluorescence of (~1.5-fold) when compared to 10 μm-LR particles. The results of this study are also corroborated by the fluorescence imaging results depicting the escape of 10 μm-LR particles from macrophage uptake (Figure 7A). These results indicate that spherical particles were readily internalized as compared to rod-shaped particles, indicating that particle shape plays a vital role in macrophage uptake.

The enhanced internalization of free DOX in the macrophages can be attributed to the rapid passive diffusion of DOX across the cell membrane [40,83]. However, DOX-conjugated 10 μm particles (both spheres and stretched particles) may undergo energy-dependent uptake, such as phagocytosis, and therefore display a comparatively reduced uptake as compared to

DOX [19]. The results further demonstrate that a change in particle shape from sphere to rod results in reduced uptake by macrophages. This is in agreement with several studies which reported that macrophage uptake is highly influenced by particle shape, where spherical particles are readily internalized as compared to those with a non-spherical shape [31,32,34]. This effect is further enhanced for particles with a higher aspect ratio, where macrophages are not able to completely engulf such particles due to the incomplete formation of actin pseudopods around the particles, then resulting in reduced cellular internalization [32,84]. Therefore, particles with a higher aspect ratio (10 μm-LR particles, in this study) possess a greater ability to escape macrophage uptake.

4.0 Conclusion

In this study we demonstrated the interplay between particle size and particle shape on the aerodynamic properties and alveolar macrophage uptake of model microparticles with different aspect ratios. Our results demonstrated that a change in the particle shape, from spherical to rod-shape, improved the aerodynamic behavior of particles, and this effect was amplified among particles with a large equivalent diameter. Additionally, for the same equivalent diameter particle, an increase in the aspect ratio resulted in improved aerodynamic properties. The current study also provides evidence that the particle shape influences cytotoxicity and cellular internalization by macrophages, which is the major clearance mechanism present in the lungs. These results also demonstrated a reduced cytotoxic activity of rod-shaped particles as compared to spherical particles. Subsequently, we assessed the influence of particle shape on the escape of phagocytic uptake by murine macrophages where rod-shape particles observed reduced uptake compared to spherical particles. Additionally, an increase in the aspect ratio of particles resulted in a decrease in internalization by macrophages. Therefore, our findings provide valuable insights into the influence of particle shape on the design of inhalable delivery carriers for pulmonary administration to combat respiratory diseases. While this is one of the first studies to demonstrate the impact of polymeric particles shape in preferential lung deposition, in order to be clinically relevant, these observations need to be translated to biodegradable polymeric particles. Future follow-up studies with this project involve developing biodegradable (PLGA) rod-shaped particles with tunable surface modifications for providing desired therapeutic effects.

Supplementary Material

Refer to Web version on PubMed Central for supplementary material.

Acknowledgments and Disclosures

5.0 References

[1]. Ruge CA, Kirch J, Lehr C-M, Pulmonary drug delivery: from generating aerosols to overcoming biological barriers—therapeutic possibilities and technological challenges, The Lancet Respiratory Medicine. 1 (2013) 402–413. 10.1016/S2213-2600(13)70072-9. [PubMed: 24429205]

[2]. Effros RM, Anatomy, development, and physiology of the lungs, GI Motility Online. (2006). 10.1038/gimo73.

[3]. Upton R, Doolette D, Kinetic Aspects of Drug Disposition in the Lungs, Clinical and Experimental Pharmacology and Physiology. 26 (1999) 381–391. 10.1046/j.1440-1681.1999.03048.x. [PubMed: 10386226]

[4]. Buckley A, Warren J, Hodgson A, Marczylo T, Ignatyev K, Guo C, Smith R, Slow lung clearance and limited translocation of four sizes of inhaled iridium nanoparticles, Particle and Fibre Toxicology. 14 (2017) 5. 10.1186/s12989-017-0185-5. [PubMed: 28187746]

[5]. Henning A, Schneider M, Nafee N, Muijs L, Rytting E, Wang X, Kissel T, Grafahrend D, Klee D, Lehr C-M, Influence of Particle Size and Material Properties on Mucociliary Clearance from the Airways, Journal of Aerosol Medicine and Pulmonary Drug Delivery. 23 (2010) 233–241. 10.1089/jamp.2009.0806. [PubMed: 20500091]

[6]. Heyder J, Deposition of Inhaled Particles in the Human Respiratory Tract and Consequences for Regional Targeting in Respiratory Drug Delivery, Proceedings of the American Thoracic Society. 1 (2004) 315–320. 10.1513/pats.200409-046TA. [PubMed: 16113452]

[7]. Edwards DA, Large Porous Particles for Pulmonary Drug Delivery, Science. 276 (1997) 1868–1872. 10.1126/science.276.5320.1868. [PubMed: 9188534]

[8]. Ungaro F, d'Emmanuele di Villa Bianca R, Giovino C, Miro A, Sorrentino R, Quaglia F, La Rotonda MI, Insulin-loaded PLGA/cyclodextrin large porous particles with improved aerosolization properties: In vivo deposition and hypoglycaemic activity after delivery to rat lungs, Journal of Controlled Release. 135 (2009) 25–34. 10.1016/j.jconrel.2008.12.011. [PubMed: 19154761]

[9]. Patel B, Gupta V, Ahsan F, PEG–PLGA based large porous particles for pulmonary delivery of a highly soluble drug, low molecular weight heparin, Journal of Controlled Release. 162 (2012) 310–320. 10.1016/j.jconrel.2012.07.003. [PubMed: 22800582]

[10]. Benne N, van Duijn J, Kuiper J, Jiskoot W, Slütter B, Orchestrating immune responses: How size, shape and rigidity affect the immunogenicity of particulate vaccines, Journal of Controlled Release. 234 (2016) 124–134. 10.1016/j.jconrel.2016.05.033. [PubMed: 27221070]

[11]. Anselmo AC, Zhang M, Kumar S, Vogus DR, Menegatti S, Helgeson ME, Mitragotri S, Elasticity of Nanoparticles Influences Their Blood Circulation, Phagocytosis, Endocytosis, and Targeting, ACS Nano. 9 (2015) 3169–3177. 10.1021/acsnano.5b00147. [PubMed: 25715979]

[12]. Schuster BS, Suk JS, Woodworth GF, Hanes J, Nanoparticle diffusion in respiratory mucus from humans without lung disease, Biomaterials. 34 (2013) 3439–3446. 10.1016/j.biomaterials.2013.01.064. [PubMed: 23384790]

[13]. Cui J, Björnmalm M, Ju Y, Caruso F, Nanoengineering of Poly(ethylene glycol) Particles for Stealth and Targeting, Langmuir. 34 (2018) 10817–10827. 10.1021/acs.langmuir.8b02117. [PubMed: 30132674]

[14]. Tang BC, Dawson M, Lai SK, Wang Y-Y, Suk JS, Yang M, Zeitlin P, Boyle MP, Fu J, Hanes J, Biodegradable polymer nanoparticles that rapidly penetrate the human mucus barrier, PNAS. 106 (2009) 19268–19273. 10.1073/pnas.0905998106. [PubMed: 19901335]

[15]. Nemmar A, Hoylaerts MF, Hoet PHM, Vermylen J, Nemery B, Size effect of intratracheally instilled particles on pulmonary inflammation and vascular thrombosis, Toxicology and Applied Pharmacology. 186 (2003) 38–45. 10.1016/S0041-008X(02)00024-8. [PubMed: 12583991]

[16]. Takeuchi I, Taniguchi Y, Tamura Y, Ochiai K, Makino K, Effects of l-leucine on PLGA microparticles for pulmonary administration prepared using spray drying: Fine particle fraction and phagocytotic ratio of alveolar macrophages, Colloids and Surfaces A: Physicochemical and Engineering Aspects. 537 (2018) 411–417. 10.1016/j.colsurfa.2017.10.047.

[17]. Mousseau F, Berret J-F, The role of surface charge in the interaction of nanoparticles with model pulmonary surfactants, Soft Matter. 14 (2018) 5764–5774. 10.1039/C8SM00925B. [PubMed: 29989135]

[18]. El-Sherbiny IM, El-Baz NM, Yacoub MH, Inhaled nano- and microparticles for drug delivery, Global Cardiology Science and Practice. 2015 (2015) 2. 10.5339/gcsp.2015.2. [PubMed: 26779496]

[19]. Mohning MP, Thomas SM, Barthel L, Mould KJ, McCubbrey AL, Frasch SC, Bratton DL, Henson PM, Janssen WJ, Phagocytosis of microparticles by alveolar macrophages during acute lung injury requires MerTK, American Journal of Physiology-Lung Cellular and Molecular Physiology. 314 (2017) L69–L82. 10.1152/ajplung.00058.2017. [PubMed: 28935638]

[20]. Prashar A, Bhatia S, Tabatabaeiyazdi Z, Duncan C, Garduño RA, Tang P, Low DE, Guyard C, Terebiznik MR, Mechanism of invasion of lung epithelial cells by filamentous Legionella pneumophila, Cell Microbiol. 14 (2012) 1632–1655. 10.1111/j.1462-5822.2012.01828.x. [PubMed: 22727141]

[21]. Dalia AB, Weiser JN, Minimization of bacterial size allows for complement evasion and is overcome by the agglutinating effect of antibody, Cell Host Microbe. 10 (2011) 486–496. 10.1016/j.chom.2011.09.009. [PubMed: 22100164]

[22]. Melin M, Trzci ski K, Meri S, Käyhty H, Väkeväinen M, The capsular serotype of Streptococcus pneumoniae is more important than the genetic background for resistance to complement, Infect Immun. 78 (2010) 5262–5270. 10.1128/IAI.00740-10. [PubMed: 20855513]

[23]. Yang DC, Blair KM, Salama NR, Staying in Shape: the Impact of Cell Shape on Bacterial Survival in Diverse Environments, Microbiol. Mol. Biol. Rev80 (2016) 187–203. 10.1128/MMBR.00031-15. [PubMed: 26864431]

[24]. Lippmann M, Effects of fiber characteristics on lung deposition, retention, and disease., (n.d.) 7.

[25]. Mossman BT, Lippmann M, Hesterberg TW, Kelsey KT, Barchowsky A, Bonner JC, Pulmonary Endpoints (Lung Carcinomas and Asbestosis) Following Inhalation Exposure to Asbestos, J Toxicol Environ Health B Crit Rev. 14 (2011) 76–121. 10.1080/10937404.2011.556047. [PubMed: 21534086]

[26]. Wright MD, Buckley AJ, Smith R, Estimates of carbon nanotube deposition in the lung: improving quality and robustness, Inhalation Toxicology. 32 (2020) 282–298. 10.1080/08958378.2020.1785594. [PubMed: 32689844]

[27]. Shams M, Ahmadi G, Rahimzadeh H, Transport and deposition of flexible fibers in turbulent duct flows, Journal of Aerosol Science. 32 (2001) 525–547. 10.1016/S0021-8502(00)00099-9.

[28]. Sturm R, A Computer Model for the Simulation of Nonspherical Particle Dynamics in the Human Respiratory Tract, Physics Research International. 2012 (2012) e142756. 10.1155/2012/142756.

[29]. Sturm R, Hofmann W, A computer program for the simulation of fiber deposition in the human respiratory tract, Computers in Biology and Medicine. 36 (2006) 1252–1267. 10.1016/j.compbiomed.2005.07.004. [PubMed: 16212953]

[30]. Löndahl J, Möller W, Pagels JH, Kreyling WG, Swietlicki E, Schmid O, Measurement Techniques for Respiratory Tract Deposition of Airborne Nanoparticles: A Critical Review, J Aerosol Med Pulm Drug Deliv. 27 (2014) 229–254. 10.1089/jamp.2013.1044. [PubMed: 24151837]

[31]. Champion JA, Mitragotri S, Shape Induced Inhibition of Phagocytosis of Polymer Particles, Pharm Res. 26 (2009) 244–249. 10.1007/s11095-008-9626-z. [PubMed: 18548338]

[32]. Doshi N, Mitragotri S, Macrophages Recognize Size and Shape of Their Targets, PLoS One. 5 (2010). 10.1371/journal.pone.0010051.

[33]. Geng Y, Dalhaimer P, Cai S, Tsai R, Tewari M, Minko T, Discher DE, Shape effects of filaments versus spherical particles in flow and drug delivery, Nature Nanotechnology. 2 (2007) 249–255. 10.1038/nnano.2007.70.

[34]. Champion JA, Mitragotri S, Role of target geometry in phagocytosis, PNAS. 103 (2006) 4930–4934. 10.1073/pnas.0600997103. [PubMed: 16549762]

[35]. Möller J, Luehmann T, Hall H, Vogel V, The Race to the Pole: How High-Aspect Ratio Shape and Heterogeneous Environments Limit Phagocytosis of Filamentous Escherichia coli Bacteria by Macrophages, Nano Lett. 12 (2012) 2901–2905. 10.1021/nl3004896. [PubMed: 22591454]

[36]. Gog JR, Murcia A, Osterman N, Restif O, McKinley TJ, Sheppard M, Achouri S, Wei B, Mastroeni P, Wood JLN, Maskell DJ, Cicuta P, Bryant CE, Dynamics of Salmonella infection of macrophages at the single cell level, Journal of The Royal Society Interface. 9 (2012) 2696–2707. 10.1098/rsif.2012.0163.

[37]. Paul D, Achouri S, Yoon Y-Z, Herre J, Bryant CE, Cicuta P, Phagocytosis Dynamics Depends on Target Shape, Biophys. J. 105 (2013) 1143–1150. 10.1016/j.bpj.2013.07.036. [PubMed: 24010657]

[38]. Champion JA, Katare YK, Mitragotri S, Making polymeric micro- and nanoparticles of complex shapes, Proc. Natl. Acad. Sci. U.S.A 104 (2007) 11901–11904. 10.1073/pnas.0705326104. [PubMed: 17620615]

[39]. Champion JA, Mitragotri S, Shape Induced Inhibition of Phagocytosis of Polymer Particles, Pharm Res. 26 (2009) 244–249. 10.1007/s11095-008-9626-z. [PubMed: 18548338]

[40]. Wang L, Song Y, Parikh A, Joyce P, Chung R, Liu L, Afinjuomo F, Hayball JD, Petrovsky N, Barclay TG, Garg S, Doxorubicin-Loaded Delta Inulin Conjugates for Controlled and Targeted Drug Delivery: Development, Characterization, and In Vitro Evaluation, Pharmaceutics. 11 (2019) 581. 10.3390/pharmaceutics11110581.

[41]. Elbatanony RS, Parvathaneni V, Kulkarni NS, Shukla SK, Chauhan G, Kunda NK, Gupta V, Afatinib-loaded inhalable PLGA nanoparticles for localized therapy of non-small cell lung cancer (NSCLC)—development and in-vitro efficacy, Drug Deliv. and Transl. Res (2020). 10.1007/s13346-020-00802-8.

[42]. Vaidya B, Kulkarni NS, Shukla SK, Parvathaneni V, Chauhan G, Damon JK, Sarode A, Garcia JV, Kunda N, Mitragotri S, Gupta V, Development of inhalable quinacrine loaded bovine serum albumin modified cationic nanoparticles: Repurposing quinacrine for lung cancer therapeutics, International Journal of Pharmaceutics. 577 (2020) 118995. 10.1016/j.ijpharm.2019.118995. [PubMed: 31935471]

[43]. Shukla SK, Kulkarni NS, Farrales P, Kanabar DD, Parvathaneni V, Kunda NK, Muth A, Gupta V, Sorafenib Loaded Inhalable Polymeric Nanocarriers against Non-Small Cell Lung Cancer, Pharm Res. 37 (2020) 67. 10.1007/s11095-020-02790-3. [PubMed: 32166411]

[44]. Abdelrahim ME, Chrystyn H, Aerodynamic Characteristics of Nebulized Terbutaline Sulphate Using the Next Generation Impactor (NGI) and CEN Method, Journal of Aerosol Medicine and Pulmonary Drug Delivery. 22 (2009) 19–28. 10.1089/jamp.2008.0650. [PubMed: 19392586]

[45]. Wang X, Parvathaneni V, Shukla SK, Kulkarni NS, Muth A, Kunda NK, Gupta V, Inhalable resveratrol-cyclodextrin complex loaded biodegradable nanoparticles for enhanced efficacy against non-small cell lung cancer, International Journal of Biological Macromolecules. 164 (2020) 638–650. 10.1016/j.ijbiomac.2020.07.124. [PubMed: 32693132]

[46]. Shukla SK, Kulkarni NS, Chan A, Parvathaneni V, Farrales P, Muth A, Gupta V, Metformin-Encapsulated Liposome Delivery System: An Effective Treatment Approach against Breast Cancer, Pharmaceutics. 11 (2019). 10.3390/pharmaceutics11110559.

[47]. Parvathaneni V, Goyal M, Kulkarni NS, Shukla SK, Gupta V, Nanotechnology Based Repositioning of an Anti-Viral Drug for Non-Small Cell Lung Cancer (NSCLC), Pharm Res. 37 (2020) 123. 10.1007/s11095-020-02848-2. [PubMed: 32514688]

[48]. Shukla SK, Chan A, Parvathaneni V, Gupta V, Metformin-loaded chitosomes for treatment of malignant pleural mesothelioma – A rare thoracic cancer, International Journal of Biological Macromolecules. 160 (2020) 128–141. 10.1016/j.ijbiomac.2020.05.146. [PubMed: 32445818]

[49]. Kauffman MK, Kauffman ME, Zhu H, Jia Z, Li YR, Fluorescence-Based Assays for Measuring Doxorubicin in Biological Systems, React Oxyg Species (Apex). 2 (2016) 432–439. 10.20455/ros.2016.873. [PubMed: 29707647]

[50]. Cooley M, Sarode A, Hoore M, Fedosov DA, Mitragotri S, Sen Gupta A, Influence of particle size and shape on their margination and wall-adhesion: implications in drug delivery vehicle design across nano-to-micro scale, Nanoscale. 10 (2018) 15350–15364. 10.1039/C8NR04042G. [PubMed: 30080212]

[51]. Missirlis D, Kawamura R, Tirelli N, Hubbell JA, Doxorubicin encapsulation and diffusional release from stable, polymeric, hydrogel nanoparticles, European Journal of Pharmaceutical Sciences. 29 (2006) 120–129. 10.1016/j.ejps.2006.06.003. [PubMed: 16904301]

[52]. Manocha B, Margaritis A, Controlled Release of Doxorubicin from Doxorubicin/-Polyglutamic Acid Ionic Complex, Journal of Nanomaterials. 2010 (2010) e780171. 10.1155/2010/780171.

[53]. Ren M, Frimmel FH, Abbt-Braun G, Multi-cycle photocatalytic degradation of bezafibrate by a cast polyvinyl alcohol/titanium dioxide (PVA/TiO2) hybrid film, Journal of Molecular Catalysis A: Chemical. 400 (2015) 42–48. 10.1016/j.molcata.2015.02.004.

[54]. Ding J, Xue G, Dai Q, Cheng R, Glass transition temperature of polystyrene microparticles, Polymer. 34 (1993) 3325–3327. 10.1016/0032-3861(93)90412-4.

[55]. Rieger J, The glass transition temperature of polystyrene, Journal of Thermal Analysis. 46 (1996) 965–972. 10.1007/BF01983614.

[56]. Shankaranarayanan JS, Kanwar JR, AL-Juhaishi AJA, Kanwar RK, Doxorubicin Conjugated to Immunomodulatory Anticancer Lactoferrin Displays Improved Cytotoxicity Overcoming Prostate Cancer Chemo resistance and Inhibits Tumour Development in TRAMP Mice, Scientific Reports. 6 (2016) 32062. 10.1038/srep32062. [PubMed: 27576789]

[57]. Vigevani A, Williamson MJ, Doxorubicin, in: Analytical Profiles of Drug Substances, Elsevier, 1981: pp. 245–274. 10.1016/S0099-5428(08)60143-4.

[58]. Das G, Nicastri A, Coluccio ML, Gentile F, Candeloro P, Cojoc G, Liberale C, De Angelis F, Di Fabrizio E, FT-IR, Raman, RRS measurements and DFT calculation for doxorubicin, Microsc. Res. Tech (2010) NA–NA. 10.1002/jemt.20849.

[59]. Samra ZQ, Ahmad S, Javeid M, Dar N, Aslam MS, Gull I, Ahmad MM, ANTICANCER MEDICINES (DOXORUBICIN AND METHOTREXATE) CONJUGATED WITH MAGNETIC NANOPARTICLES FOR TARGETING DRUG DELIVERY THROUGH IRON, Preparative Biochemistry and Biotechnology. 43 (2013) 781–797. 10.1080/10826068.2013.782042. [PubMed: 23876138]

[60]. Hermán V, Takacs H, Duclairoir F, Renault O, Tortai JH, Viala B, Core double–shell cobalt/graphene/polystyrene magnetic nanocomposites synthesized by in situ sonochemical polymerization, RSC Adv. 5 (2015) 51371–51381. 10.1039/C5RA06847A.

[61]. Fang J, Xuan Y, Li Q, Preparation of polystyrene spheres in different particle sizes and assembly of the PS colloidal crystals, Science China-Technological Sciences - SCI CHINA-TECHNOL SCI. 53 (2010) 3088–3093. 10.1007/s11431-010-4110-5.

[62]. Mansur AAP, Carvalho SM, Lobato ZIP, de F. Leite M, da S. Cunha A, Mansur HS, Design and Development of Polysaccharide-Doxorubicin-Peptide Bioconjugates for Dual Synergistic Effects of Integrin-Targeted and Cell-Penetrating Peptides for Cancer Chemotherapy, Bioconjugate Chem. 29 (2018) 1973–2000. 10.1021/acs.bioconjchem.8b00208.

[63]. Ji Y, Yang X, Ji Z, Zhu L, Ma N, Chen D, Jia X, Tang J, Cao Y, DFT-Calculated IR Spectrum Amide I, II, and III Band Contributions of N-Methylacetamide Fine Components, ACS Omega. 5 (2020) 8572–8578. 10.1021/acsomega.9b04421. [PubMed: 32337419]

[64]. Peng T, Liu K, Gao L, Gao L, Chen J, Wang J, Liu Y, Wang Y, Yan Z, Yu L, Poly (l-γ-glutamylglutamine) Polymer Enhances Doxorubicin Accumulation in Multidrug Resistant Breast Cancer Cells, Molecules. 21 (2016) 720. 10.3390/molecules21060720.

[65]. Chun C, Lee SM, Kim CW, Hong K-Y, Kim SY, Yang HK, Song S-C, Doxorubicin–polyphosphazene conjugate hydrogels for locally controlled delivery of cancer therapeutics, Biomaterials. 30 (2009) 4752–4762. 10.1016/j.biomaterials.2009.05.031. [PubMed: 19520429]

[66]. Borghardt JM, Kloft C, Sharma A, Inhaled Therapy in Respiratory Disease: The Complex Interplay of Pulmonary Kinetic Processes, Canadian Respiratory Journal. 2018 (2018) e2732017. 10.1155/2018/2732017.

[67]. Pleasants RA, Hess DR, Aerosol Delivery Devices for Obstructive Lung Diseases, Respiratory Care. 63 (2018) 708–733. 10.4187/respcare.06290. [PubMed: 29794206]

[68]. Marple VA, Roberts DL, Romay FJ, Miller NC, Truman KG, Van Oort M, Olsson B, Holroyd MJ, Mitchell JP, Hochrainer D, Next Generation Pharmaceutical Impactor (A New Impactor for Pharmaceutical Inhaler Testing). Part I: Design, Journal of Aerosol Medicine. 16 (2003) 283–299. 10.1089/089426803769017659. [PubMed: 14572326]

[69]. Copley Scientific Next Generation Impactor (NGI) Model 170, 5.950,00 € Copley Scientific Next Generation Impactor (NGI) Model 170, 5.950,00 € (n.d.). https://profcontrol.de/Copley-Scientific-Next-Generation-Impactor-NGI-Model-170_1 (accessed March 12, 2019).

[70]. Carvalho TC, Peters JI, Williams RO, Influence of particle size on regional lung deposition – What evidence is there?, International Journal of Pharmaceutics. 406 (2011) 1–10. 10.1016/j.ijpharm.2010.12.040. [PubMed: 21232585]

[71]. Tsuda A, Henry FS, Butler JP, Particle Transport and Deposition: Basic Physics of Particle Kinetics, in: Comprehensive Physiology, American Cancer Society, 2013: pp. 1437–1471. 10.1002/cphy.c100085.

[72]. Martonen TB, Katz IM, Deposition Patterns of Aerosolized Drugs Within Human Lungs: Effects of Ventilatory Parameters, Pharm Res. 10 (1993) 871–878. 10.1023/A:1018913311788. [PubMed: 8321856]

[73]. Lippmann M, Yeates DB, Albert RE, Deposition, retention, and clearance of inhaled particles., Br J Ind Med. 37 (1980) 337–362. [PubMed: 7004477]

[74]. Darquenne C, Deposition Mechanisms, Journal of Aerosol Medicine and Pulmonary Drug Delivery. 33 (2020) 181–185. 10.1089/jamp.2020.29029.cd. [PubMed: 32598200]

[75]. Darquenne C, Aerosol Deposition in Health and Disease, J Aerosol Med Pulm Drug Deliv. 25 (2012) 140–147. 10.1089/jamp.2011.0916. [PubMed: 22686623]

[76]. Wang J, Bhattacharyya J, Mastria E, Chilkoti A, A quantitative study of the intracellular fate of pH-responsive doxorubicin-polypeptide nanoparticles, J Control Release. 260 (2017) 100–110. 10.1016/j.jconrel.2017.05.032. [PubMed: 28576641]

[77]. Li M, Tang Z, Lin J, Zhang Y, Lv S, Song W, Huang Y, Chen X, Synergistic antitumor effects of doxorubicin-loaded carboxymethyl cellulose nanoparticle in combination with endostar for effective treatment of non-small-cell lung cancer, Adv Healthc Mater. 3 (2014) 1877–1888. 10.1002/adhm.201400108. [PubMed: 24846434]

[78]. He L, Liang H, Lin L, Shah BR, Li Y, Chen Y, Li B, Green-step assembly of low density lipoprotein/sodium carboxymethyl cellulose nanogels for facile loading and pH-dependent release of doxorubicin, Colloids and Surfaces B: Biointerfaces. 126 (2015) 288–296. 10.1016/j.colsurfb.2014.12.024. [PubMed: 25576811]

[79]. Etrych T, Subr V, Laga R, Ríhová B, Ulbrich K, Polymer conjugates of doxorubicin bound through an amide and hydrazone bond: Impact of the carrier structure onto synergistic action in the treatment of solid tumours, Eur J Pharm Sci. 58 (2014) 1–12. 10.1016/j.ejps.2014.02.016. [PubMed: 24632485]

[80]. Gao Q, Han X, Zhu J, Chen R, Sun B, A polymer–drug conjugate for doxorubicin: Synthesis and biological evaluation of pluronic F127-doxorubicin amide conjugates, Journal of Applied Polymer Science. 124 (2012) 4953–4960. 10.1002/app.35613.

[81]. Yu Y, Chen C-K, Law W-C, Sun H, Prasad PN, Cheng C, A degradable brush polymer–drug conjugate for pH-responsive release of doxorubicin, Polym. Chem6 (2015) 953–961. 10.1039/C4PY01194E.

[82]. Mahesh S, Tang K-C, Raj M, Amide Bond Activation of Biological Molecules, Molecules. 23 (2018). 10.3390/molecules23102615.

[83]. Munerati M, Cortesi R, Ferrari D, Di Virgilio F, Nastruzzi C, Macrophages loaded with doxorubicin by ATP-mediated permeabilization: potential carriers for antitumor therapy, Biochim Biophys Acta. 1224 (1994) 269–276. 10.1016/0167-4889(94)90200-3. [PubMed: 7981242]

[84]. Chatterjee N, Yang J, Kim S, Joo SW, Choi J, Diameter size and aspect ratio as critical determinants of uptake, stress response, global metabolomics and epigenetic alterations in multi-wall carbon nanotubes, Carbon. 108 (2016) 529–540. 10.1016/j.carbon.2016.07.031.

Highlights

1. Bioinspired particles of desired size were successfully fabricated using 1-dimensional film stretching method.

2. Particle shape of inhalable carriers governed their aerodynamic properties and deposition behavior in lungs.

3. Macrophage uptake and viability was considerably influenced by the shape of the delivery carriers

4. Particle shape could serve as a promising biophysical parameter for designing of effective inhalable delivery carriers
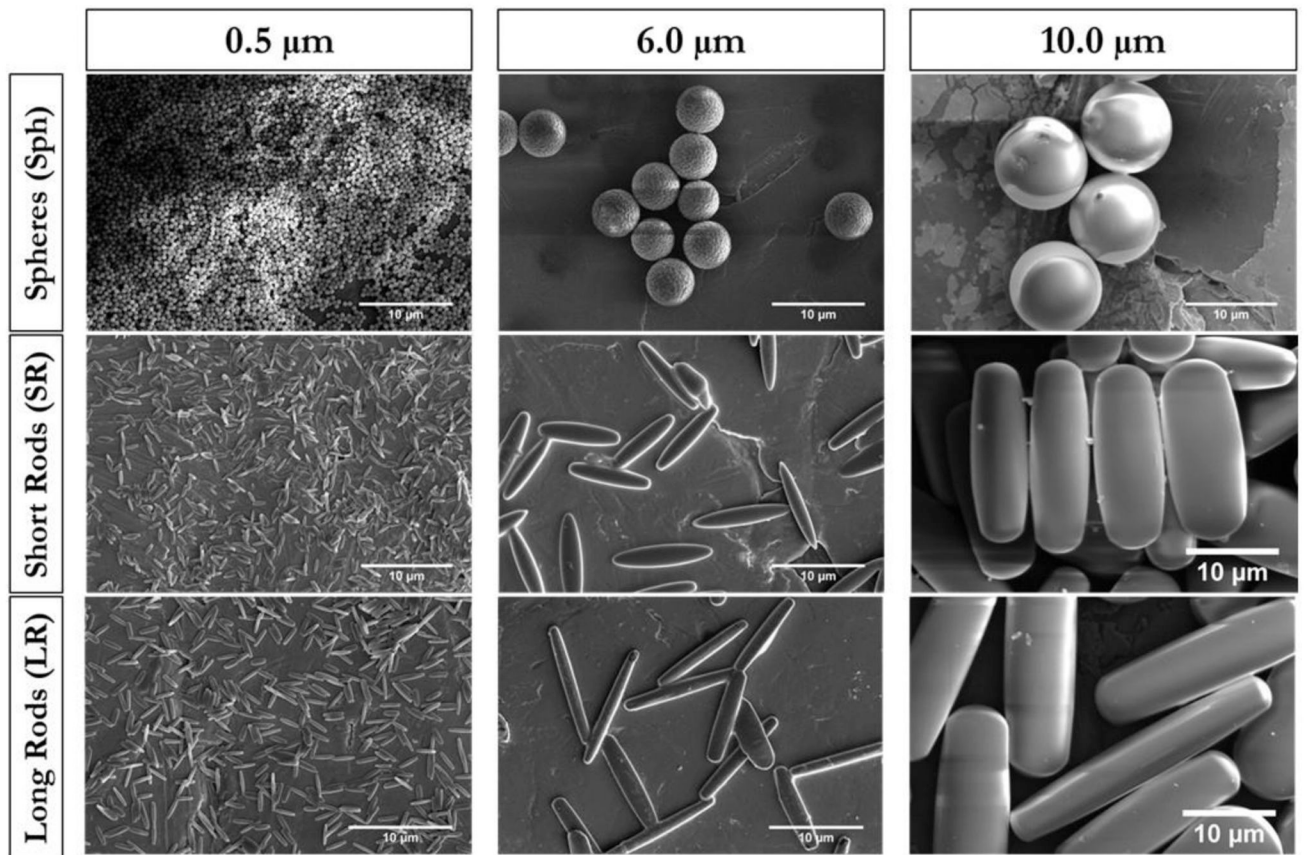
Figure 1:
(A) Schematic representation of fabrication of particles of varied shapes using the stretching method. (B) Reaction scheme for conjugation of DOX to the carboxylic groups present on the surface of the polystyrene particles using EDC-NHS chemistry.

Figure 2:
Representative scanning electron microscopy (SEM) micrographs of particles obtained by stretching microparticles of various sizes. Scale bar= 10μm
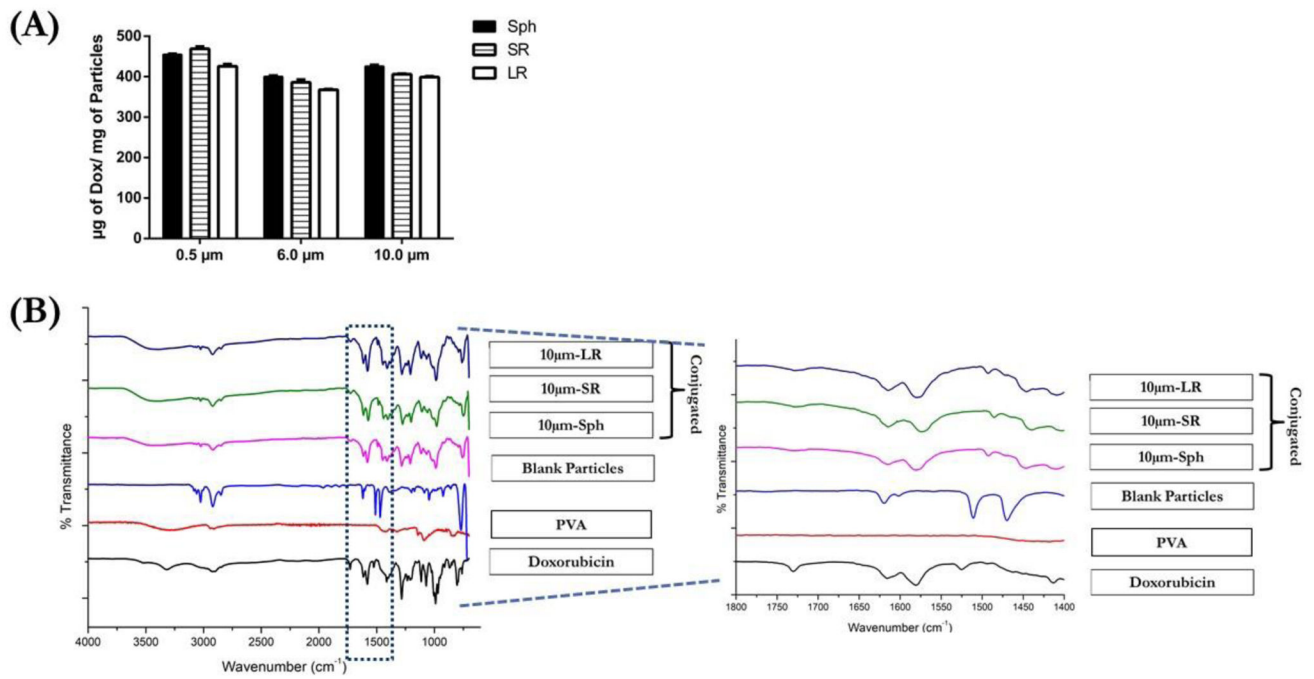
Figure 3:
Characterization of DOX conjugation to various 10μm particles. (A) amount of DOX-conjugated to various particles expressed as μg of Dox/mg of particles. Data is represented as mean±SD for n=3 experiments. (C) Spectra of samples analyzed using FT-IR also a representative magnified image of spectra is shown for all the samples.
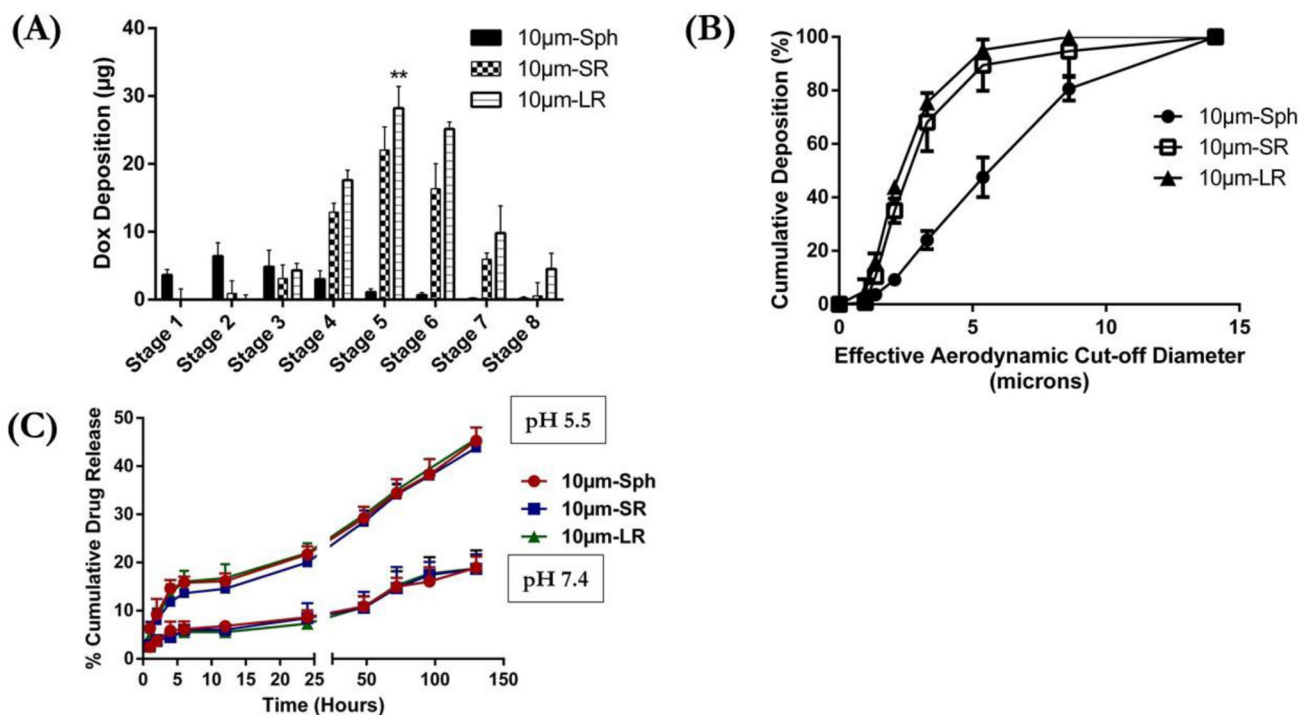
Figure 4:
(A) Aerodynamic distribution pattern of various 10μm particles at different stages of Next Generation Cascade Impactor (NGI) expressed as DOX Deposition (μg) at each stage. (B) % Cumulative deposition plotted against effective cut-off diameter (μm) to determine deposition impact due to difference in particle shape of 10μm particle. (C) *In-vitro* drug release profile of DOX from various 10μm particles; 10μm-Sph, 10μm-SR and 10μm-LR evaluated at pH 7.4 and pH 5.5. Data represents mean ± SD (n=3). ** $p<0.01$.

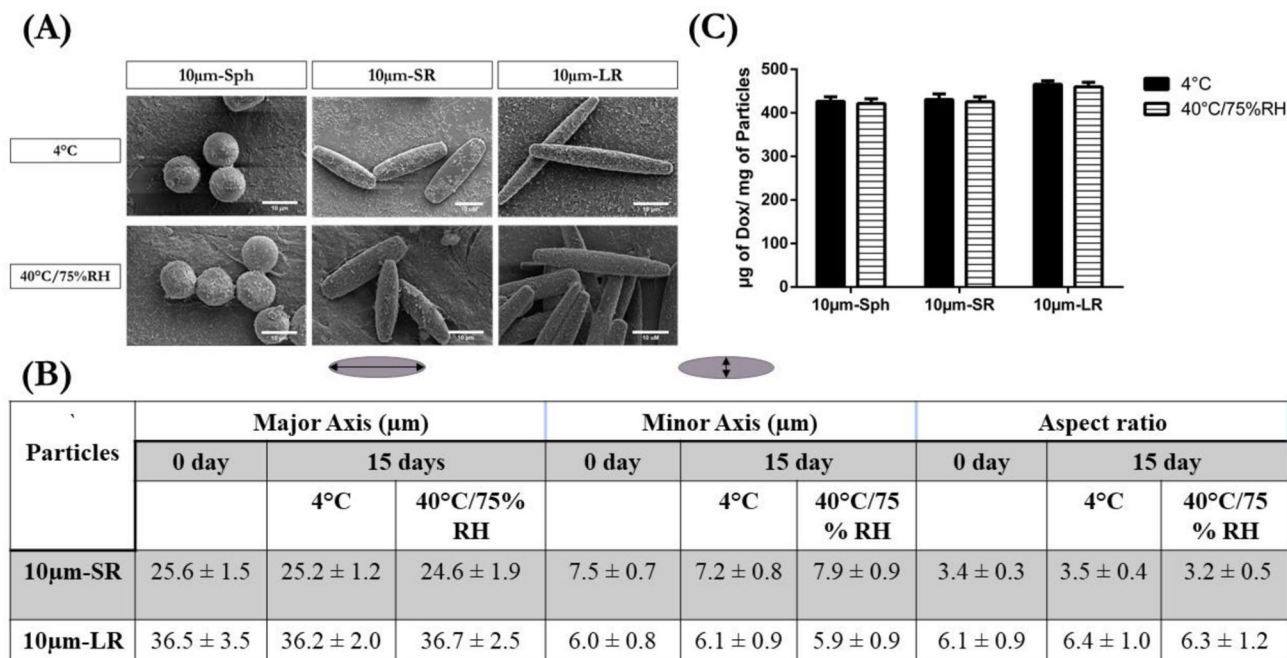| Particles	Major Axis (μm)			Minor Axis (μm)			Aspect ratio		
	0 day	15 days		0 day	15 day		0 day	15 day	
		4°C	40°C/75% RH		4°C	40°C/75 % RH		4°C	40°C/75 % RH
10μm-SR	25.6 ± 1.5	25.2 ± 1.2	24.6 ± 1.9	7.5 ± 0.7	7.2 ± 0.8	7.9 ± 0.9	3.4 ± 0.3	3.5 ± 0.4	3.2 ± 0.5
10μm-LR	36.5 ± 3.5	36.2 ± 2.0	36.7 ± 2.5	6.0 ± 0.8	6.1 ± 0.9	5.9 ± 0.9	6.1 ± 0.9	6.4 ± 1.0	6.3 ± 1.2

Figure 5:

Stability of various 10μm particles evaluated at two different conditions; 4°C and 40°C/ 75%RH, after 15 days storage evaluated for changes in morphology, particle size, and amount of drug conjugated. (A) Stability evaluated in terms of morphological changes of particles represented by respective SEM micrographs. (B) Stability evaluated in terms of major axis length, minor axis length and aspect ratio of particles and (C) Stability evaluated in terms of μg of Dox/mg of particles present at the end of 15 days.
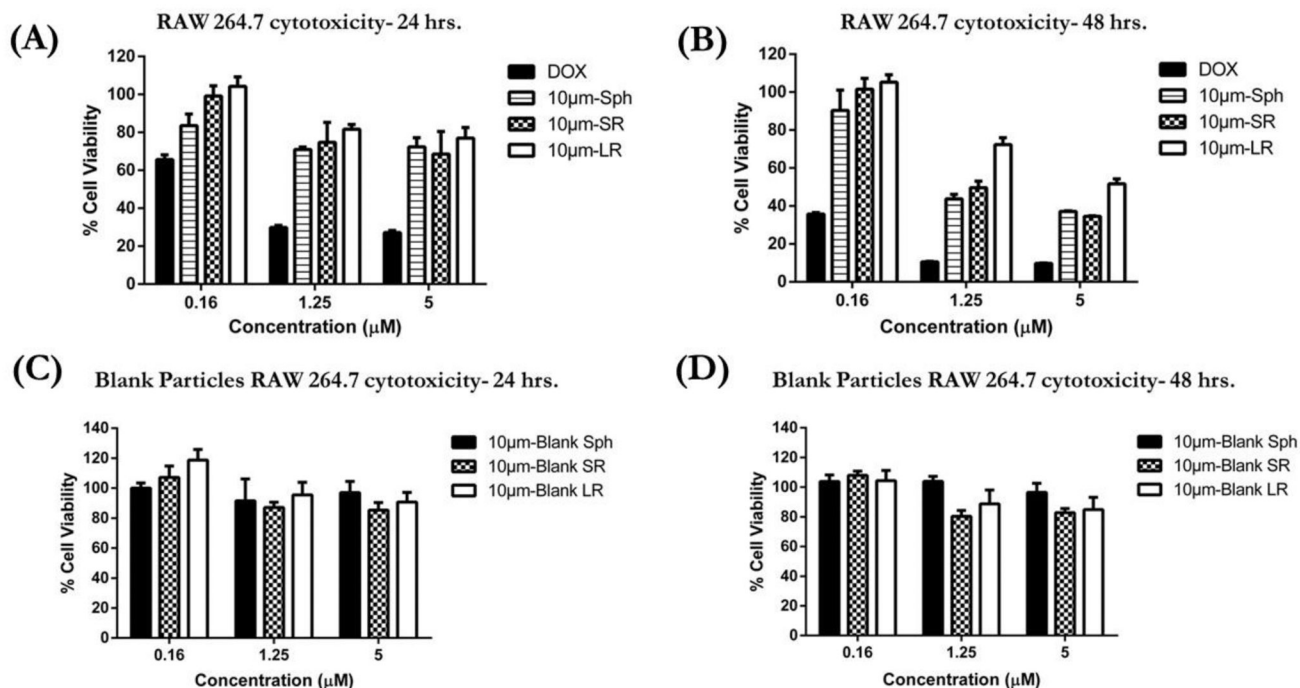
Figure 6:

In-vitro cytotoxicity studies of various 10μm particles in RAW 264.7 cells determined using MTT assay. (A) Cytotoxic potential of DOX-conjugated 10μm particles evaluated after 24 hours incubation (B) Cytotoxic potential of DOX-conjugated 10μm particles was evaluated after 48 hours incubation (C) Blank particle cytotoxicity evaluated in RAW 264.7 cells after 24 hours incubation and (D) Blank particle cytotoxicity evaluated in RAW 264.7 cells after 48 hours incubation. (Data represent mean ± SD of 3 individual experiments with n=6 for each experiment).
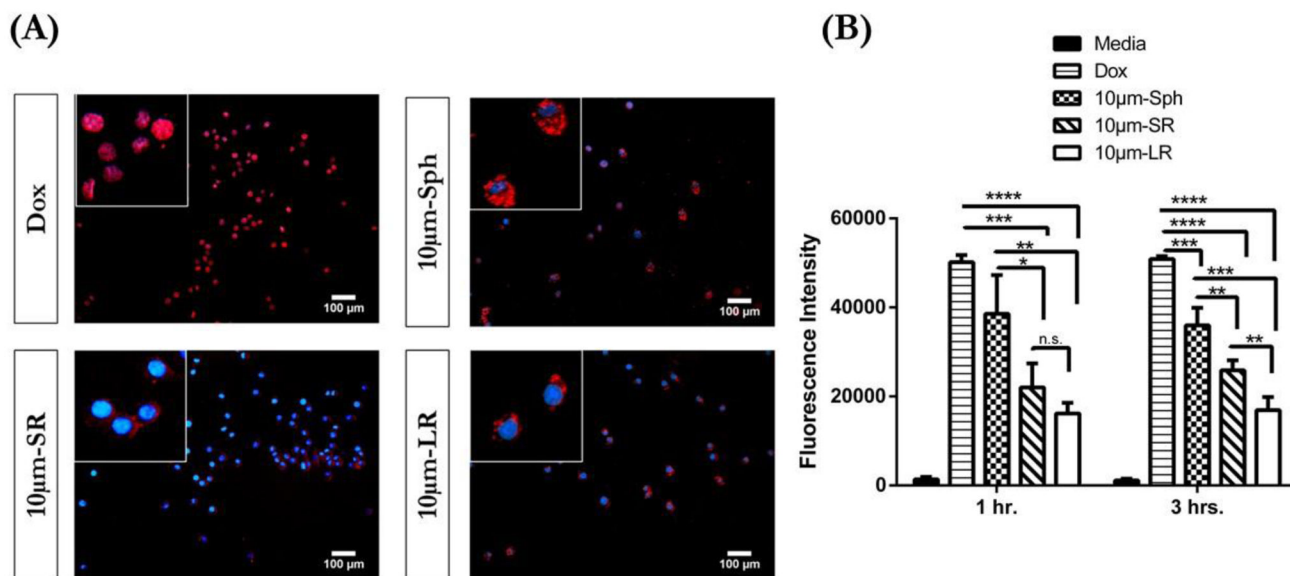
Figure 7:

In-vitro cellular uptake studies of various 10μm particles. (A) Florescent images of Dox, 10μm-Sph, 10μm-SR and 10μm-LR in RAW 264.7 macrophages after 3 hours incubation. The inset images represent magnified image of the outside image. Representative images from n = 3 experiments. Scale bar = 100 μm (B) Quantitative determination of intracellular DOX after 1 hr. and 3 hours incubation in RAW 264.7 cells represented as florescence intensity. Data represent mean ± SD (n=3). *p<0.05, ** p<0.01, *** p<0.001 and **** p<0.0001.*

Table 1:

Calculated particle size of stretched particles using Image J software.

Sample	Major Axis (μm)	Minor Axis (μm)	Aspect Ratio (AR) (Major Axis/Minor Axis)
0.5μm-SR	1.4 ± 0.1	0.3 ± 0.0	4.1 ± 0.2
0.5μm-LR	1.9 ± 0.2	0.3 ± 0.0	6.6 ± 0.6
6.0μm-SR	9.1 ± 0.9	1.7 ± 0.3	5.4 ± 0.8
6.0μm-LR	13.7 ± 1.6	1.5 ± 0.4	9.1 ± 1.4
10μm-SR	22.1 ± 3.3	7.1 ± 0.9	3.3 ± 0.5
10μm-LR	32.2 ± 3.2	5.6 ± 0.9	5.8 ± 1.1

Data represent mean±SD for 3 individual images of each sample with n=30 for each image (Total of 90 images/sample).

Table 2:

Aerosolization properties of various microparticles calculated in terms of MMAD and % FPF.

Sample	MMAD	% FPF
0.5μm-Sph	4.5 ± 0.3	77.2 ± 5.0
0.5μm-SR	4.2 ± 0.5	74.2 ± 0.7
0.5μm-LR	4.4 ± 0.4	79.5 ± 5.7
6.0μm-Sph	5.6 ± 0.1	61.7 ± 2.1
6.0μm-SR	4.3 ± 0.2 [**]	76.5 ± 4.9 [*]
6.0μm-LR	4.7 ± 0.1 [**]	76.2 ± 1.1 [*]
10μm-Sph	8.2 ± 0.8	44.7 ± 5.7
10μm-SR	4.2 ± 0.6 [****]	89.5 ± 9.6 [***]
10μm-LR	3.4 ± 0.1 [****]	95.5 ± 0.6 [****]

Data are represented as mean±SD for n=3 experiments.

[*]
p<0.05,

[**]
p<0.01,

[***]
p<0.001 and

[****]
p<0.0001.

Table 3:

IC$_{50}$ values of different treatment groups in RAW 264.7 cells calculated from experimental cytotoxicity data obtained after 48 hours incubation.

Treatment Group	IC$_{50}$ value (μM)
Dox	0.1 ± 0.0
10μm-Sph	2.8 ± 0.8
10μm-SR	3.1 ± 0.1
10μm-LR	7.5 ± 3.1